Chinese Chemical Letters 35 (2024) 109524

Contents lists available at ScienceDirect

Chinese Chemical Letters

journal homepage: www.elsevier.com/locate/cclet

In-situ fabrication of $TiO_2/NH_2-MIL-125(Ti)$ *via* MOF-driven strategy to promote efficient interfacial effects for enhancing photocatalytic NO removal activity

Maosen Xu[a], Pengfei Zhu[a], Qinghong Cai[a], Meichun Bu[a], Chenghua Zhang[b,*], Hong Wu[a], Youzhou He[a,*], Min Fu[a], Siqi Li[c], Xingyan Liu[a,*]

[a] *Chongqing Key Laboratory of Catalysis and New Environmental Materials, College of Environment and Resources, Chongqing Technology and Business University, Chongqing 400067, China*
[b] *School of Pharmacy, North Sichuan Medical College, Nanchong 637100, China*
[c] *State Key Joint Laboratory of Environment Simulation and Pollution Control, School of Environment, Tsinghua University, Beijing 100084, China*

ARTICLE INFO

Article history:
Received 28 September 2023
Revised 28 December 2023
Accepted 14 January 2024
Available online 18 January 2024

Keywords:
Photocatalysis
NH_2-MIL-125(Ti)
TiO_2
NO removal
ROS

ABSTRACT

Deep oxidation of NO molecules to nitrate species by photocatalysis with virtually no toxic byproduct NO_2 generation is a challenging task. In this study, TiO_2 *in-situ* grows based on $NH_2-MIL-125(Ti)$ (NM-125) not only inhibited TiO_2 agglomeration, but also contacted more tightly to obtain efficient interfacial effects, thus displaying excellent photocatalytic NO removal activity (68.08%). The formation of TiO_2 is directly confirmed by characterizations such as X-ray diffraction (XRD), transmission electron microscope (TEM), X-ray photoelectron spectroscopy (XPS). Meanwhile, UV–vis, photoluminescence, and photoelectrochemical analysis indicate that TiO_2 formation effectively improves the optical properties. Moreover, the strong electron interaction and electron transport direction between NM-125 and TiO_2 are investigated by density functional theoretical (DFT) calculation. Finally, combined with the results of electron spin resonance (ESR) and *in-situ* FT-IR test, the intermediate processes of NO adsorption and photocatalytic oxidation reaction are discussed in depth, where the production of reactive oxygen species (ROS) under light is the key factor in the successful degradation of NO. Compared with NM-125 which can only produce $^{\cdot}OH$ through photogenerated electrons since the lower valence band position, NMT-2 can directly produce $^{\cdot}OH$ through photogenerated holes, thereby relieving the pressure on photogenerated electrons and producing more ROS. This study will provide reasonable guidance for the modification of NM-125 for photocatalytic removal of ppb-level NO.

© 2024 Published by Elsevier B.V. on behalf of Chinese Chemical Society and Institute of Materia Medica, Chinese Academy of Medical Sciences.

Nitrogen oxides (NO_x, mainly NO) are of the typical air pollutants, which are the main culprits for environmental problems such as photochemical haze, acid rain, and ozone hole [1–3]. Therefore, a number of methods have been reported to selective sequester or transform NO, including physical/chemical adsorption [4], heterogeneous catalytic reduction [5] and oxidation [6], *etc.* But these methods are always used for dealing with relatively high concentrations NO, which become financial and energy constraints in the purification of ppb-level NO. However, photocatalytic oxidation is an environment-friendly and easy approach to removing NO at ppb-level [7–10]. Therefore, photocatalysis technology is seen as an ideal tool for air purification, and it is of great significance to explore new high-efficiency photocatalysts to achieve ppb-level NO removal.

Metal-organic frameworks (MOFs) materials are a novel type of porous organic–inorganic hybrid supramolecular material, which has high surface areas, tunable pores, and versatile chemical functionalities [11,12]. More importantly, MOFs can exhibit photocatalytic behavior under visible light irradiation, which has attracted much attention in recent decades. Due to the diversity of existing metal ions and organic linkers, MOF materials with corresponding target applications can be reasonably developed. Particularly, $NH_2-MIL-125(Ti)$ (NM-125) has been studied as a visible-light photocatalyst for dye degradation, hydrogen production, CO_2 reduction, *etc.* [13]. However, the photocatalytic activity is still limited by the finite visible light absorption capacity and the high photogenerated carrier recombination rate [14,15]. To solve the

* Corresponding authors.
E-mail addresses: zchua@nsmc.edu.cn (C. Zhang), yzhectbu@163.com (Y. He), xyliuctbu@126.com (X. Liu).

https://doi.org/10.1016/j.cclet.2024.109524
1001-8417/© 2024 Published by Elsevier B.V. on behalf of Chinese Chemical Society and Institute of Materia Medica, Chinese Academy of Medical Sciences.

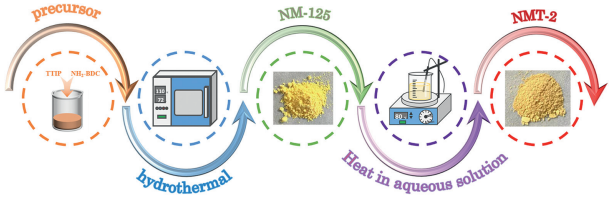

Scheme 1. *In-situ* fabrication of TiO_2 and NM-125 heterojunction.

above issues, heterojunction coupling, regulating metal clusters, and incorporation of catalytic active sites that have been adopted to adjust the optical properties of NM-125 [16–18]. Among these strategies, enhancing photocatalytic activity by constructing heterojunctions with other semiconductor materials is undoubtedly one of the simplest ways, but what method can be used to prepare a heterojunction structure with excellent activity and stability is worth exploring.

Recently, TiO_2 photocatalyst has been extensively investigated and has commercial application in the field of photocatalytic NO removal due to its high redox ability and stability under light illumination. However, there are still serious problems that hinder its further application in air purification [19]. For example, pure TiO_2 particles tend to aggregate, which leads to weakened adsorption capacity and reduced active site utilization [20]. To overcome these problems, we report a MOF-driven TiO_2 generation strategy that uses the Ti-O clusters exposed by NM-125 loss of ligands in aqueous solutions at higher temperatures to *in-situ* grow TiO_2 particles (Scheme 1). In this case, the generated TiO_2 will be well dispersed in the NM-125 framework, which can not only enhance the photocatalytic activity of the TiO_2 itself but also extend the lifetime of photogenerated carriers due to the strong interfacial effects between NM-125 and TiO_2. Most notably, compared with TiO_2 and NM-125 heterojunction prepared by other synthetic methods, this strategy has more advantages, because the Ti source of TiO_2 is directly originated from NM-125, so the TiO_2/NM-125 are more closely contacted, which is not only conducive to rapid charge transfer at the interface, but also has better stability.

In Fig. 1a, the X-ray diffraction (XRD) pattern of NM-125 is the same as that reported in the previous literature, indicating that NM-125 has been successfully prepared [21,22]. However, as the heat treatment temperature increased from 70 °C to 90 °C, the corresponding characteristic peak of NM-125 gradually decreased, while the characteristic peak of TiO_2 (JCPDS card No. 84–1286) appeared and the intensity increased with the temperature increase, which can be caused by Ti-O clusters exposed after the heat treatment ligand decarbonization at higher temperatures to *in-situ* grow TiO_2 particles. The presence of ligand defects in the structure of MOFs is directly confirmed by TGA characterization analysis (Fig. S1 in Supporting information). More notably, the characteristic peak of TiO_2 is significantly wider, which can be the TiO_2 obtained through this way displays poor crystallinity as the uniform dispersion in the NM-125 framework.

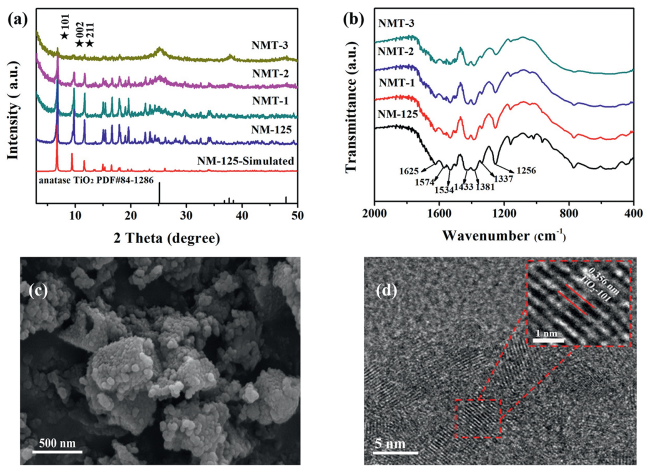

Fig. 1. (a) XRD patterns and (b) FT-IR spectra of NM-125 and NMT-X. (c) SEM and (d) HRTEM images of NMT-2.

The Fourier transform infrared (FT-IR) spectra of NMT-X are similar to those of the original NM-125, indicating that the generation of TiO_2 has a weak effect on the NM-125 (Fig. 1b). The peak at 1625 cm^{-1} corresponds to the N–H bending vibration of the aromatic amine, while the peaks at 1337 cm^{-1} and 1256 cm^{-1} belong to the C–N stretching vibration. The peaks at 1574 cm^{-1} and 1381 cm^{-1} correspond to the symmetric vibrations of the carboxylate connectors, and the peak of 1534 cm^{-1} and 1433 cm^{-1} correspond to the asymmetric vibration [23–26]. Bands in the 400–800 cm^{-1} region match the vibrations of Ti-O [27,28]. It is not difficult to find that when the heat treatment temperature increases, the characteristic peaks of carboxyl functional groups around 1600–1400 cm^{-1} weaken, and the corresponding peaks of Ti-O clusters of 400–800 cm^{-1} also gradually weaken. This is due to the loss of organic ligands leading to carboxyl functional group shedding to expose more Ti-O clusters which convert to TiO_2 particles at a certain temperature.

In Fig. S3 (Supporting information), the morphologies of NM-125 presents a thin and disk-like shape, which is consistent with previous reports [29–31]. Interestingly, NMT-2 displays a similar morphology to NM-125, but a lot of small particles appear on the surface, which is caused by the production of TiO_2 (Fig. 1c). It can be found that lots of TiO_2 particles are evenly wrapped on the surface of MOF, which also proves our previous idea that TiO_2 formed by MOF-driven can well inhibit TiO_2 agglomeration. In order to better explain the presence of TiO_2 in the MOF framework, transmission electron microscope (TEM) tests are carried out. The lattice spacing of 0.356 nm in NMT-2 can be identified, corresponding to the (101) crystal plane of TiO_2, which is almost consistent with the JCPDS card No. 84–1286 simulation value (Fig. 1d).

In order to further investigate the impact of TiO_2 generation on the original MOF, the high-resolution XPS spectra of the samples are described in Figs. 2a-d, and the binding energy and atomic concentration of the corresponding peaks are shown in Tables S1 and S2 (Supporting information). Through in-depth observation of the high-resolution O 1s spectrum, it can be found that the content of C=O significantly decreased from 60.79% to 30.61%, while the content of Ti-O increased accordingly, from 32.67% to 61.82%. This phenomenon is understandable based on the production of TiO_2. Under a certain temperature of aqueous solution, NM-125 loses organic ligands, resulting in Ti-O cluster exposure and conversion to TiO_2 particles. More importantly, the N 1s, C 1s, Ti 2p, and O 1s XPS peaks of NMT-2 shifted slightly toward lower binding energies compared to NM-125, which may be attributed to strong electronic interaction between TiO_2 and NM-125 [20]. The above results successfully indicate the formation process of TiO_2 in NM-125 and the possible existence of strong electronic interaction, which is conducive to enhancing charge flow.

DFT theoretical calculations are carried out to better study the strong electronic interaction between TiO_2 and NM-125. The ELF results indicate that there is covalent interaction between Ti atoms in TiO_2 and O atoms exposed to Ti-O clusters in NM-125, which can be used as a high-speed electron transfer channel and thus provide the possibility of free electron transfer (Fig. 2e). Meanwhile, the charge density difference is used to accurately determine the transport direction of the interface charge, where yellow and blue represent charge accumulation and charge consumption respectively (Fig. 2f). It can be clearly observed that the extra elec-

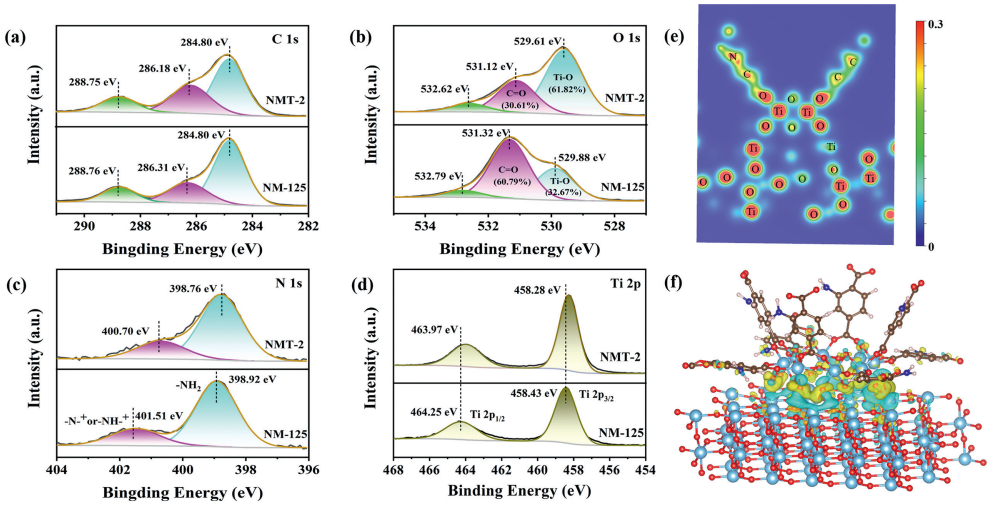

Fig. 2. XPS spectra of NM-125 and NMT-2, (a) C 1s, (b) O 1s, (c) N 1s, (d) Ti 2p. (e) Electron location function (ELF) of NMT-2. (f) Charge density difference of NMT-2. The isosurfaces are set to 0.002 eV/Å^3.

trons in TiO_2 tend to transfer to the O atoms of the Ti-O clusters exposed by NMT-2. Therefore, the prepared NMT-2 heterojunction photocatalyst has a Ti-O path of electron transfer channel. Moreover, the charge transfer direction is from TiO_2 to NM-125, so this fast charge transfer channel without destroying the crystal structure is the key reason why NMT-2 has excellent photocatalytic NO removal activity.

The UV–vis, steady-state photoluminescence (PL), and photoelectrochemical analysis are performed to probe the optical properties of samples. In Fig. S7 (Supporting information), it can be seen that with the increase of TiO_2 production, the light absorption capacity in the visible region increases, but the absorption peak corresponding to the organic ligand decreases at 400 nm. Therefore, the more TiO_2 produced also means that the more serious the destruction of NM-125, which is unfavorable to the photocatalytic reaction. Moreover, the optical band gap energy of the NM-125 sample is calculated by the equation: $ahv = A(hv - E_g)^{n/2}$, where NM-125 is estimated to be 2.39 eV, which is helpful to calculate the specific valence band position of NM-125. In Fig. S8 (Supporting information), the NMT-2 sample has the weakest fluorescence intensity at 320 nm excitation wavelength, indicating that it has the lowest photogenerated carrier recombination rate, which reflected that NMT-2 has the longest electron-hole pairs life that is a signal of superior photocatalytic activity. The photocurrent response diagram display that the photocurrent intensity of NMT-X is stronger than that of NM-125 (Fig. S9a in Supporting information). Among them, NMT-2 has the highest photocurrent intensity, indicating that it has the best separation efficiency of photogenerated carriers. In addition, the Nyquist semicircle diameter (Fig. S9b in Supporting information) of NMT-2 also exhibits the smallest radius in all samples, which indicates the surface resistance of NMT-2 is the minimum. Hence, this phenomenon is conducive to the transfer of surface charges, which also corresponded to PL characterization and photocurrent response results.

In Fig. 3a, the NO removal rate of NM-125 is only 39.72%, while the photocatalytic activity of the modified NTM-X photocatalyst is significantly enhanced, as follows: NTM-1 (60.07%) < NTM-3 (60.63%) < NTM-2 (68.07%). The TiO_2 production can significantly improve the photocatalytic NO removal activity of the original MOF because the photogenerated carriers generated by TiO_2 can be transferred to the original MOF. However, with the increase of TiO_2 production, the photocatalytic activity is significantly weakened, because the Ti source in TiO_2 comes from the Ti-O clusters exposed to the original MOF. Therefore, the more TiO_2 is produced, the more serious the damage to the original MOF, which is not conducive to improving the photocatalytic performance. In addition, in photocatalyzed NO removal reactions, it is extremely important to evaluate the concentration of the toxic by-product NO_2, as this can determine whether the photocatalyst converts all NO to nitrate species instead of NO_2 (Fig. 3b). Surprisingly, the concentration of NO_2 for both NM-125 and NMT-X materials is below 15 ppb, which indicates that the prepared photocatalyst can break through the energy barrier of the conversion of toxic by-product NO_2 to NO_2^-/NO_3^-. The conversion rate of NO to NO_2 and NO_2^-/NO_3^- is calculated to further analyze the photocatalytic NO removal performance (Table S3 in Supporting information), where the NO to NO_2 conversion rate of NM-125 is slightly higher than that of NMT-X, indicating that the modified NM-125 can better inhibit the production of toxic by-product NO_2 (Fig. 3e). In addition, the NO to NO_2^-/NO_3^- conversion rate of NM-125 and NMT-X is almost close to the degradation rate of NO, which also confirms that the prepared catalysts convert almost all NO to NO_2^-/NO_3^-. More importantly, the photocatalytic NO removal activity of NMT-2 under visible light irradiation is much higher than that of commercial P25 [32], and the activity of photocatalysts reported in other literature under the same conditions is comparable (Table S4 in Supporting information).

The stable catalytic activity of the prepared photocatalyst is a key factor to evaluate its research significance, so five consecutive photocatalytic NO removal experiments are carried out to verify the stability of the material. In Figs. 3c, d and f, after five continuous photocatalytic NO removal experiments, the catalyst not only did not display deactivation, but the conversion rate of NO_2 is only 3.20%, indicating that it can steadily convert NO to low-toxic NO_2^-/NO_3^- for a long time (Table S5 in Supporting information).

The reaction between photogenerated carriers and adsorbed small molecules under light can produce reactive oxygen species (ROS), which will play a crucial role in photocatalytic reactions [33–35]. To clarify the type of ROS involved in efficient NO removal, electron spin resonance (ESR) measurements are conducted (Fig. S11 in Supporting information). The strong signals of superoxide radical ($^{\bullet}O_2^-$), hydroxyl radical ($^{\bullet}OH$), and singlet oxygen ($^1O_2$) are founded in both NM-125 and NMT-2 under visible light irradiation, indicating the involvement of $^{\bullet}O_2^-$, $^{\bullet}OH$, and $^1O_2$ in the photocatalytic reaction. Interestingly, the signal peak of NMT-2 is significantly higher than that of NM-125, which indicates that NMT-2 can produce more ROS under light illumination conditions.

In-situ FT-IR real-time monitoring is carried out to study the intermediate substances produced by photocatalyst during the adsorption reaction and photocatalytic oxidation reaction stage. Ta-

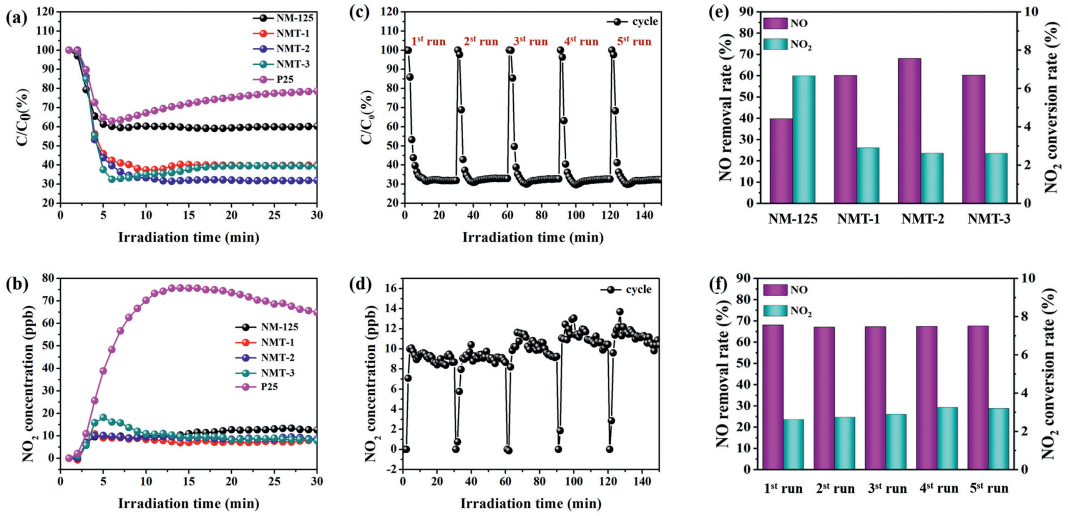

Fig. 3. (a) Photocatalytic NO removal activity and (b) NO_2 concentration during photocatalysis of NM-125, NMT-X, and P25. (c) NO removal stability tests and (d) changes in NO_2 concentration of NMT-2 under 5 consecutive experiments. (e) The comparison of NO removal rate and NO_2 conversion rate during photocatalysis. (f) The comparison of NO removal rate and NO_2 conversion rate under 5 consecutive experiments.

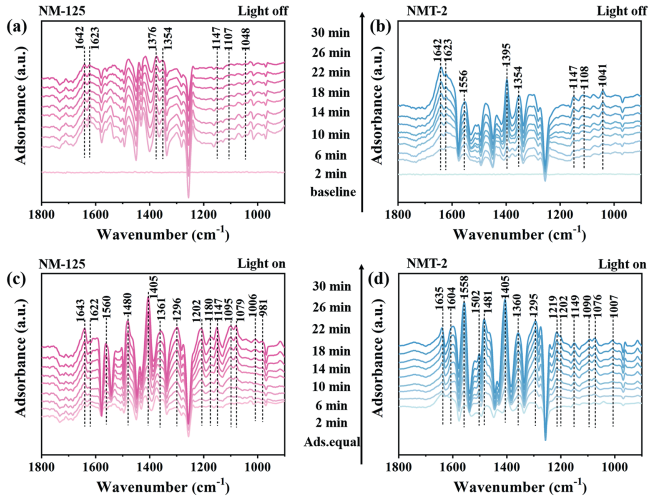

Fig. 4. *In-situ* FT-IR spectra of (a, b) NO adsorption and (c, d) reaction process over NM-125 and NMT-2.

ble S6 (Supporting information) summarizes the substances corresponding to IR peaks during NO adsorption and oxidation. During the adsorption process (Figs. 4a and b), NM-125 and NMT-2 are exposed to a mixture of NO and O_2, and the intensity of some peaks gradually increased with the extension of time. This is because NO will first be adsorbed on the catalyst surface, and the subsequent accumulation of NO will produce NO derivatives, such as NO_2, N_2O_4 [36,37]. In addition, the characteristic peak of NO^-, NO_2^- and NO_3^- is detected, which are perhaps highly active intermediates caused by the oxidizing capacity of the material itself [38,39].

After a mixture of gases (NO and O_2) is adsorbed on the photocatalyst surface for 30 min, the changes of surface adsorption species of NM-125 and NMT-2 are monitored under visible light irradiation (Figs. 4c and d). For NM-125, it can be found that most of the peaks of NO and NO derivatives (1623, 1376 cm^{-1}) produced during the adsorption stage disappear and weaken, and are converted to the peaks of NO_2^- and NO_3^- (1560, 1480, 1405 1296, 1202, 1079, 1006, 981 cm^{-1}). Moreover, the peak of NO^- (1361, 1147 cm^{-1}) present in the adsorption stage is further enhanced, perhaps because the photogenerated electrons can be directly transferred to NO [40–42]. Meanwhile, the peak of $N_2O_2^{2-}$ as an intermediate in the conversion of N_2O_4 to nitrate species is detected, which further reflected the consumption of N_2O_4 produced in the adsorption stage. For NMT-2, the reaction process is almost the same as that of NM-125, which is to convert NO and its derivatives generated during the adsorption stage into NO_2^-/NO_3^-, but it is worth noting that the species changes in the reaction of NMT-2 are more abundant and the relative intensity is higher (Fig. S12 in Supporting information). More importantly, there are still NO derivative peaks in the NM-125, which is not found in the photocatalytic reaction stage of NMT-2. These phenomena suggest that NMT-2 may have superior photocatalytic activity than NM-125 in the photocatalytic NO removal reaction, which is also well consistent with the above characterization analysis.

According to the experimental results and literature analysis, the mechanism of photogenerated carrier transport is explored. If the photogenerated carriers transfer follows the traditional heterojunction type mechanism pattern, photogenerated electrons are collected at the conduction band of TiO_2, and photogenerated holes are collected at the valence band of NM-125, in which the detailed bandgap structure of NM-125 and TiO_2 is described in Fig. S13 (Supporting information). It is not difficult to find that the photogenerated electrons collected at the conduction band of TiO_2 are unlikely to produce $^{\bullet}O_2^-$, because the conduction band position of TiO_2 is −0.24 eV than the redox potential −0.33 eV ($O_2/^{\bullet}O_2^-$) more positive. Meanwhile, it is not able to generate $^{\bullet}OH$ because the valence band position is significantly lower than +2.38 eV ($OH^-/^{\bullet}OH$). However, the signal peaks of $^{\bullet}O_2^-$ and $^{\bullet}OH$ are found in both NMT-2 photocatalysts by ESR characterization. Therefore, a Z-scheme heterojunction is more reasonable for NMT-2 composites to photocatalytic oxidation of NO (Fig. S14 in Supporting information) [20,43].

It can be speculated that there are two reaction paths between NM-125 and NMT-2, which is the main factor leading to the difference in their photocatalytic activity. Firstly, through in-depth analysis of Fig. S15 (Supporting information), the band gap structure that the valence band position of NM-125 is +1.54 eV, which is much lower than +2.38 eV ($OH^-/^{\bullet}OH$), indicating that photogenerated holes cannot oxidize OH^- to $^{\bullet}OH$. However, the peak of $^{\bullet}OH$ can be produced in the ESR test, so the $^{\bullet}OH$ is mainly produced by photogenerated electrons for the NM-125 photocatalyst based on $^{\bullet}O_2^- \rightarrow H_2O_2 \rightarrow {}^{\bullet}OH$ route [44,45]. But, for the NMT-2, OH^- can be directly oxidized to $^{\bullet}OH$ by photogenerated holes due to the

valence band position of TiO_2 at +2.86 eV. Secondly, the conduction band position of the two materials is lower than −0.33 eV (O_2/$^{\bullet}O_2^-$), which indicates that the photogenerated electrons can reduce the O_2 adsorbed on the surface of the catalyst to $^{\bullet}O_2^-$. Therefore, for the NM-125, the production of $^{\bullet}O_2^-$ and $^{\bullet}OH$ is inseparable from the role of photogenerated electrons, and for the NMT-2, this can relatively better relieve the pressure of photogenerated electrons. Finally, NM-125 and NMT-2 photocatalysts can produce $^1O_2$ under light conditions, another active oxygen substance, which is mainly produced by photogenerated holes converting $^{\bullet}O_2^-$ to $^1O_2$ [46–48]. The generation of $^1O_2$ can offset the consumption of $^{\bullet}O_2^-$ and $^{\bullet}OH$, indicating that this active substance is conducive to improving the photocatalytic NO removal rate [43,49,50]. Therefore, based on the above discussion and analysis, the reaction path between NM-125 and NTM-2 photocatalysts is accurately predicted at Scheme S1 (Supporting information).

In summary, our study is the first to prepare NMT-X Z-scheme heterojunction with excellent stability and high TiO_2 dispersion by stirring NM-125 in an aqueous solution at a certain temperature. The generation of TiO_2 promote the transport of photogenerated carriers and extended its lifetime, thus representing superior and stable photocatalytic NO removal activity (68.06%), and even in 5 continuous photocatalytic NO removal experiments, the removal rate of NO and the conversion rate of NO_2 remained basically unchanged. This means that the prepared photocatalyst can effectively transform NO and prevent the formation of toxic by-product NO_2 for a long time. Moreover, in this work, we deeply analyzed the relationship between the heterojunction construction strategy and ROS production in the reaction and clearly clarified the intermediate process of NM-125 and NMT-2 photocatalysts in the photocatalytic NO removal reaction. This work provides new insights into the modification of NM-125 and the mechanism of photocatalytic oxidation of NO.

Declaration of competing interest

The authors declare that they have no known competing financial interests or personal relationships that could have appeared to influence the work reported in this paper.

Acknowledgments

This work was supported by the National Natural Science Foundation of China (No. 22001026), Graduate Innovation Program of Chongqing Technology and Business University (No. yjscxx2023–211–38), Student Science and Technology Innovation Fund Project of Chongqing Technology and Business University (Nos. 223006, 233012).

Supplementary materials

Supplementary material associated with this article can be found, in the online version, at doi:10.1016/j.cclet.2024.109524.

References

[1] H. Wang, Y. Sun, G. Jiang, et al., Environ. Sci. Technol. 52 (2018) 1479–1487.
[2] W. Cui, J. Li, F. Dong, et al., Environ. Sci. Technol. 51 (2017) 10682–10690.
[3] Y. Wang, J. Sheng, X. Zhao, et al., Chin. Chem. Lett. 34 (2023) 107967.
[4] F. Rezaei, A.A. Rownaghi, S. Monjezi, et al., Energy Fuels 29 (2015) 5467–5486.
[5] S. Xiong, J. Weng, Y. Liao, et al., J. Phys. Chem. C 120 (2016) 15299–15309.
[6] A. Wang, Y. Guo, F. Gao, et al., Appl. Catal. B 202 (2017) 706–714.
[7] W. Cui, J. Li, W. Cen, et al., J. Catal. 352 (2017) 351–360.
[8] J. Ma, H. He, F. Liu, Appl. Catal. B 179 (2015) 21–28.
[9] H. Wang, K. Li, J. Li, et al., Environ. Sci. Technol. Lett. 8 (2021) 873–877.
[10] J. Li, X. Liu, H. Wang, et al., Chin. Chem. Lett. 35 (2024) 108596.
[11] Y. Qian, F. Zhang, H. Pang, Adv. Funct. Mater. 31 (2021) 2104231.
[12] A.E. Thorarinsdottir, T.D. Harris, Chem. Rev. 120 (2020) 8716–8789.
[13] L. Liu, S. Du, Y. Xiao, et al., Appl. Catal. B: Environ. 338 (2023) 123094.
[14] Y. Zhang, W. Cao, B. Zhu, et al., J. Colloid Interface Sci. 611 (2022) 706–717.
[15] S. Liu, X. Jiang, G.I.N. Waterhouse, et al., Sep. Purif. Technol. 294 (2022) 121094.
[16] H. Sepehrmansourie, H. Alamgholiloo, N. Noroozi Pesyan, et al., Appl. Catal. B: Environ. 321 (2023) 122082.
[17] L. Pukdeejorhor, S. Wannapaiboon, J. Berger, et al., J. Mater. Chem. A 11 (2023) 9143–9151.
[18] S. Chen, G. Hai, H. Gao, et al., Chem. Eng. J. 406 (2021) 126886.
[19] F. Yuan, R. Yang, B. Wang, et al., Sep. Purif. Technol. 312 (2023) 123423.
[20] Q. Huang, Y. Hu, Y. Pei, et al., Appl. Catal. B: Environ. 259 (2019) 118106.
[21] Y. He, Y. Tan, M. Song, et al., J. Hazard. Mater. 430 (2022) 128468.
[22] M. Xu, Y. Xu, C. Zhang, et al., Sep. Purif. Technol. 322 (2023) 124374.
[23] D. Jin, Q. Xu, L. Yu, et al., Microchim. Acta 182 (2015) 1885–1892.
[24] G. Mo, L. Wang, J. Luo, Sep. Purif. Technol. 277 (2021) 119643.
[25] Q. Jia, J. Zhou, L. Gong, et al., Mol. Catal. 530 (2022) 112599.
[26] M. Kandiah, M.H. Nilsen, S. Usseglio, et al., Chem. Mater. 22 (2010) 6632–6640.
[27] Y. Fu, M. Tan, Z. Guo, et al., Chem. Eng. J. 452 (2023) 139417.
[28] X. Zhang, Z. Chen, Y. Luo, et al., J. Hazard. Mater. 405 (2021) 124128.
[29] Y. Fu, K. Zhang, Y. Zhang, et al., Chem. Eng. J. 412 (2021) 128722.
[30] Y. Zhang, J. Song, Q. Pan, et al., J. Mater. Chem. B 8 (2019) 114–124.
[31] X.M. Cheng, X.Y. Dao, S.Q. Wang, et al., ACS Catal. 11 (2021) 650–658.
[32] B. Lei, W. Cui, J. Sheng, et al., Sci. Bull. 65 (2020) 467–476.
[33] X. Li, Z. Hu, Q. Li, et al., Chem. Commun. 56 (2020) 14195–14198.
[34] D. Ma, W. Liu, Y. Huang, et al., Environ. Sci. Technol. 56 (2022) 3678–3688.
[35] X. Dong, W. Cui, H. Wang, et al., Sci. Bull. 64 (2019) 669–678.
[36] Q. Ren, Y. He, H. Wang, et al., ACS Catal. 12 (2022) 14015–14025.
[37] F. Chang, C. Yang, X. Wang, et al., J. Clean. Prod. 380 (2022) 135167.
[38] F. Zhong, C. Yuan, Y. He, et al., J. Hazard. Mater. 438 (2022) 129463.
[39] L. Liu, P. Ouyang, Y. Li, et al., J. Hazard. Mater. 439 (2022) 129637.
[40] X. Zhou, J. Zhang, X. Wang, et al., J. Hazard. Mater. 436 (2022) 129271.
[41] F. Chang, X. Wang, C. Yang, et al., Compos. Part B: Eng. 231 (2022) 109600.
[42] P. Yan, Q. Ren, F. Zhong, et al., Chin. Chem. Lett. 33 (2022) 3161–3166.
[43] F. Chang, S. Zhao, Y. Lei, et al., J. Colloid Interface Sci. 649 (2023) 713–723.
[44] J. Li, X. Dong, Y. Sun, et al., Appl. Catal. B 226 (2018) 269–277.
[45] J. Li, X. Dong, Y. Sun, et al., Appl. Catal. B 239 (2018) 187–195.
[46] H. Wang, X. Yang, W. Shao, et al., J. Am. Chem. Soc. 137 (2015) 11376–11382.
[47] Z. He, B. Chen, Y. Li, et al., Sep. Purif. Technol. 320 (2023) 123886.
[48] S. Wang, W. Cui, B. Lei, et al., Environ. Sci. Technol. 57 (2023) 12890–12900.
[49] Y. Li, M. Gu, M. Zhang, et al., Chem. Eng. J. 389 (2020) 124421.
[50] H. Ma, W. Yang, H. Tang, et al., J. Hazard. Mater. 452 (2023) 131269.